Mathematical models of biofluid flows in compliant ducts

N. KIZILOVA[1)], M. HAMADICHE[2)], M. GAD-EL-HAK[3)]

[1)]*Department of Theoretical Mechanics*
Kharkov National University
Svobody Sq. 4, 61195 Kharkov, Ukraine
e-mail: nnk_ @bk.ru

[2)]*Laboratoire de Mécanique des Fluides et d'Acoustique*
École Centrale de Lyon
Av. Guy de Collongue 36, F69134 Ecully, France
e-mail: mahmoud.hamadiche@ec-lyon.fr

[3)]*Department of Mechanical & Nuclear Engineering*
Virginia Commonwealth University
Richmond, VA 23284-3015, U.S.A.
e-mail: gadelhak@vcu.edu

A LITERATURE REVIEW OF LIQUID AND GAS FLOWS in compliant tubes, ducts and cavities in living bodies is presented. The common features of such flows as determined by fluid–structure interactions and system instabilities are described. The corresponding mathematical models are given and theoretical and numerical results are discussed. Original new results on flow stabilization in layered viscoelastic tubes in biosystems are also presented.

Key words: biomechanics, biofluid flows, distensible tubes, flow stability, sound generation.

AMS Subject Classification: 74F10.

1. Introduction

BIOFLUID FLOWS IN DISTENSIBLE TUBES, fluid–structure interaction and flow-induced instabilities represent a subject of many review papers [1–7]. The book edited by PEDLEY and CARPENTER [8] also contains several useful reviews. A wide range of experimental and theoretical considerations of the problem is available in the literature. Results obtained by numerical simulations for membrane-like structures are reviewed in [3, 5] and more recently in [6]. Experimental studies of collapsible tubes are reviewed in [9] and new experimental results are obtained in [10]. Though many physical and physiological phenomena of flow instability in collapsed and non-collapsed tubes are explained, the prob-

lem is still of great interest for numerous technical and biomedical applications, medical diagnostics chief amongst them.

Blood flows in normal and pathologically changed arteries and veins – through stenosis, aneurisms, stents and grafts – have common features with air flows in nasal cavities and upper airways in snorers, glottis, larynx and vertebrate lungs. The main irregularities of such flows can be described by mathematical models of fluid flow over viscoelastic surfaces with complex mechanical properties. In the present paper, a survey of recent data on biofluid flow instabilities in distensible tubes and the related physical phenomena are given, and some novel results obtained by the present authors are reported. The new results focus on analyzing multilayer thick-tube models.

2. Physical phenomena in compliant tubes

The accepted model of physiological flows in collapsible tubes is the 'Starling resistor' proposed in [11] as a model of the peripheral blood circulation. It consists of a segment of pliable tube mounted axially between two rigid tubes and enclosed in a pressurized chamber (Fig. 1a). In experiments using different steady controlling parameters, a remarkable variety of unsteady behavior of the system can be observed, including highly nonlinear oscillations, transitions and hystereses between different oscillatory regimes, and chaotic behavior. Flowrate limitation is observed when the internal pressure is sufficiently low to cause collapse at the downstream end of the compliant tube, so that the flowrate becomes substantially pressure-independent. The dynamics of the collapsible tube depends on the coupling between the fluid and the wall via the constitutive tube law, which is generally nonlinear. Prior to tube's collapse, any decrease in downstream pressure accelerates the fluid. In a collapsed state, in contrast, the tube's
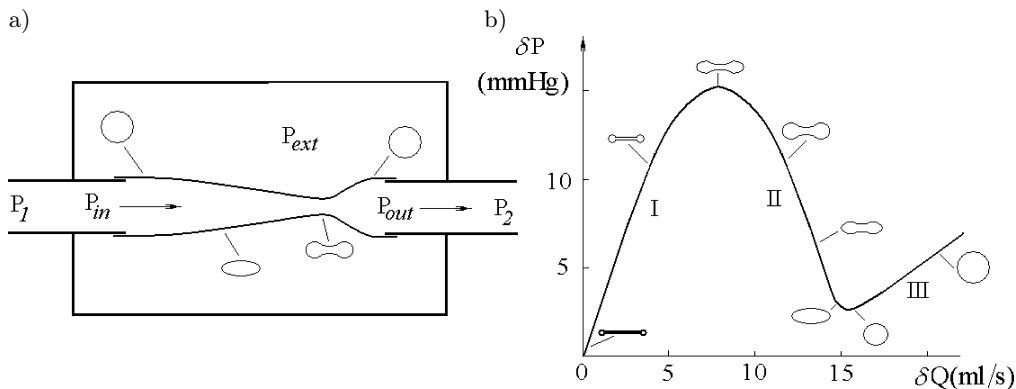
Fig. 1. a) Schematic of experiments with Starling resistor. b) Typical dependency $\delta P(Q)$ for the passive blood vessel. The corresponding cross-sectional shapes are depicted along the branches I, II and III of the curve.

neck narrows, and a point at which the volume flowrate attains its peak value is reached. The collapsed part (neck) is typically found near the downstream end of the tube, and past that neck the fluid motion is essentially three-dimensional with turbulent mixing and flow separation, and the shear stress at the wall is changed in comparison with the non-collapsible state.

Flow limitation is mostly associated with small-amplitude noise-like fluctuations of the downstream pressure because it is seldom accompanied by large-amplitude self-excited oscillations. The latter is mostly exhibited only during the transition to or from maximum flow to the flow-limited state. Large-amplitude self-excited oscillations can be observed when the external pressure in the chamber is increased. When external pressure is being reduced to certain level, either flow limitation or absence of tube collapse can be obtained for the same values of the upstream transmural pressures P_{tm} [12]. The onset of oscillations has been examined in order to determine the lowest Reynolds number at which the oscillations appear. In all the experiments, large-amplitude flow-induced oscillations have been detected at Re $\geq$ 200 [10, 13, 14].

Laboratory experiments on flow limitation at Re $>$ 250 commonly reveal self-excited oscillations and noise generation, which are believed to be linked, i.e. high-Reynolds-number flow limitation is accompanied by wall oscillations [15,16]. At relatively low Reynolds numbers, wall oscillations are unattainable and flow limitation is determined by viscous pressure drop. It is however not clear what is the extent at which self-excited oscillations accompany the flow-rate limitation. For example, flow limitation without wall oscillation has been observed in [12,16]. As it was found in some early experiments [17], the outbreak of spontaneous oscillations coincides with the fluid speed reaching the critical pressure wave speed, and interconnection of the flow limitation and the wall oscillations has been hypothesized. An analogy to the choking condition of gas dynamics has been made to explain the flow-limitation phenomenon in collapsible urethra [18, 19]. As it was shown theoretically, the instabilities leading to flutter could arise at lower fluid speeds [20], and subcritical oscillations at low downstream resistance have also been found [21].

Physiological observations are in agreement with laboratory experiments. Increased blood flow after a physical or thermal load often produces some noise that can be detected over the large blood vessels. Air flow during forced expiration is accompanied by wheezing, and registration of the generated sound as well as differentiation between dry and moist rales is important for diagnostics. Occurrence of flow-induced oscillations can be explained by analogy to sonic gas flows. Noise generation is possible when fluid moves through a distensible tube and the flow becomes sonic (flow velocity equal to the speed of low-frequency pressure waves). When the tube is mounted vertically and the flow is directed downwards, flow-induced oscillations are determined by the hydraulic jump conditions [22]. An

important physiological problem for both upward and downward flows in vertical distensible tubes is illustrated by flow in the blood vessels of the neck, especially for long-necked animals such as giraffes [23]. In that case, flow instability and vein collapse are of great importance for the blood supply to the brain.

3. Mathematical models of distensible tubes

The lumped-parameter model has been used to explain the physical phenomena observed when a fluid flows through a Starling resistor [23, 24]. The model consists of a series connection of two rigid tubes with fixed volumes and a distensible one between them. The Windkessel model [25] for collapsible tubes is presented by the mass balance equation

$$(3.1) \qquad \frac{dV_2}{dt} = Q_{12} - Q_{23},$$

where $V_2(t)$ is the volume of the distensible tube, Q_{12} and Q_{23} are respectively inflow from the first tube and outflow into the third one. Expressions for Q_{12} and Q_{23} as functions of pressure drops are usually taken from the Poiseuille law. The cross-section area $A^*(t)$ and pressure $P^*(t)$ in the narrowest part of the tube's neck, input and output pressures $P_{in}(t)$, $P_{out}(t)$, flowrates $Q_{in}(t)$, $Q_{out}(t)$, and tube's compliance $C_2(P_2) = dV_2/dP_2$ are introduced, which result in a nonlinear system of ODE for the pressure, flowrate and tube's cross-section. The resulting second-, third- [24–26] and fifth-order [27] systems of ODE describe oscillations of the respective parameters and have been used to explain the experimental observations.

The wave propagation phenomena and different types of oscillatory instability can be successfully described by one-dimensional models [1, 28–31]. The mass continuity and momentum equations for a Newtonian fluid are respectively

$$(3.2) \qquad \frac{\partial A}{\partial t} + \frac{\partial (AU)}{\partial x} = 0,$$

$$(3.3) \qquad \rho_f \left(\frac{\partial U}{\partial t} + U \frac{\partial U}{\partial x} \right) = -\frac{\partial P}{\partial x} - \tau_w(A),$$

where $P(t, x)$ and $U(t, x)$ are, respectively, mean pressure and velocity, $\tau_w(A)$ is the wall shear stress per unit length of the tube, and ρ_f is the fluid density.

Since the shear stress depends on the derivative of velocity with respect to the radial coordinate while the one-dimensional models include the longitudinal coordinate only, the expression for $\tau_w(A)$ is often taken from the steady Poiseuille flow in circular or elliptical cross-section tubes [28, 31] depending on the relationship between A and A_0, and the area of the nonstretched tube at $P_{tm} = 0$. Thus,

$$(3.4) \qquad \tau_w(A) = \begin{cases} \dfrac{8\pi\mu U}{A}, & A < A_0, \\[2mm] \dfrac{4\pi\mu\alpha_1}{AA_0\alpha_2}\left(\left(\dfrac{A_0}{A\alpha_2}\right)^2 + 1\right), & A \geq A_0, \end{cases}$$

where α_1 and α_2 are empirical constants, which are different for the non-collapsed and collapsed portions of the tube.

The steady flow relationship $\tau_w(A)$ can also be taken from the Womersley model [32] of pulsatile flow in distensible tubes in the form [33]:

$$(3.5) \qquad \tau_w(A) = -\frac{\rho_f}{\sqrt{\pi A}}\left(\frac{8c_v\pi\mu U}{\rho_f} + (c_v - 1)\frac{\partial(UA)}{\partial t}\right).$$

The experimental $P(A)$ curves for blood vessels (curve 1 in Fig. 2a) can be approximated by either the simple linear relation

$$(3.6) \qquad P - P_{ext} = \lambda(A - A_0),$$

where the slope λ is different in the collapsed and non-collapsed states (curve 2 in Fig. 2b) or by the nonlinear relationship [28]:

$$(3.7) \qquad P(S) = \begin{cases} k\left(1 - \left(\dfrac{A_0}{A}\right)^{3/2}\right), & A < A_0, \\[2mm] \alpha_3 k\left(\dfrac{A}{A_0} - 1\right), & A \geq A_0, \end{cases}$$
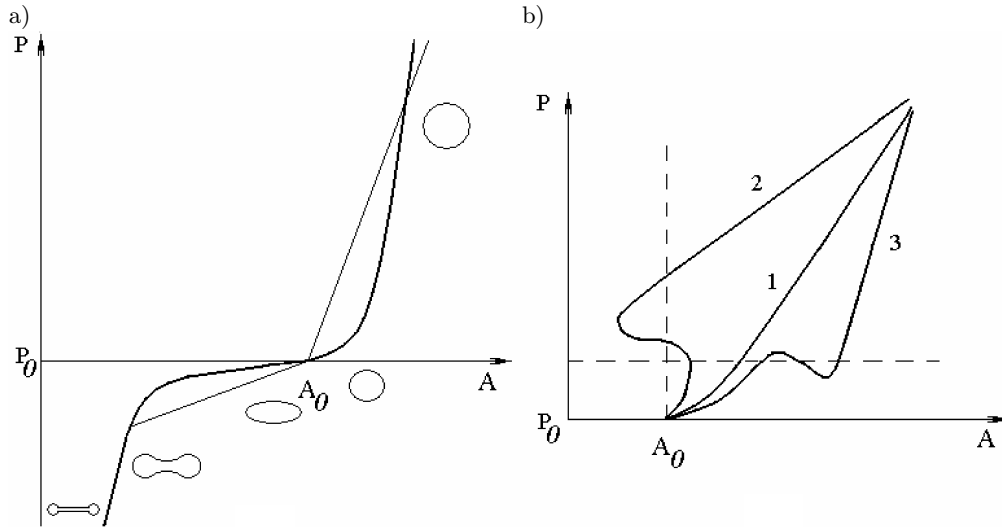
Fig. 2. Experimental dependencies $P(S)$ for a) passive and b) active tubes at different flow conditions; 1: monotonically increasing, unambiguous dependency; 2: S-shape curve; 3: N-shape curve.

where λ is the wall elasticity coefficient, k is the circumferential bending stiffness of the tube, and α_3 is an empirical coefficient.

The relationship between the transmural pressure $P_{tm}(t,x) = P - P_{ext}$ and the cross-sectional area $A(t,x)$, the tube law, has also been used in the nonlinear form [34]:

$$(3.8) \qquad P - P_{ext} = \frac{Gh_0}{R_0}\left(1 - \left(\frac{A_0}{A}\right)^2\right),$$

where G is the Young's modulus of the wall material, h is the wall thickness, and subscript 0 corresponds to the state with $P_{tm} = 0$.

Along the collapsed part of the tube, dA/dx changes its sign. For the tube with longitudinal stretching T, the collapsed part can be modeled by two membranes and the pressure variation due to the membrane's curvature can be taken into account in the tube law [1]:

$$(3.9) \qquad P = P_{ext} + P(A) - T\frac{d^2A}{dx^2}.$$

When the outer surface of the tube is attached to the surrounding media, which is the case for arteries and veins, the pressure dependence on area is valid for both small and large deformations and is empirically determined to be [34]:

$$(3.10) \qquad P - P_{ext} = \frac{kGh_0}{\sqrt{A}}\left(\left(\frac{A}{A_0}\right)^{1/2} - \left(\frac{A_0}{A}\right)^{3/2}\right).$$

Finally, the one-dimensional problem with the tube law $P - P_{ext} = \Theta(A)$ in any of the above-mentioned forms of $\Theta(A)$ gives a hyperbolic system of equations, whose solution can be obtained as a superposition of forward and backward propagating waves [1,28–34]. The effects of longitudinal wall tension and energy loss due to flow separation and the stability of steady flow are respectively investigated in [35, 36]. Depending on the model parameters, it is shown that a compliant tube may be unstable to at least three different oscillation modes with different frequencies. This is consistent with a complex dynamical behavior of the fluid–structure system. The motion of the separation point is found to be important in connection with wall oscillations.

In the tube laws such as Eqs. (3.6), (3.7), (3.8) or (3.10), the changes in $A(t,x)$ with pressure variations $P(t,x)$ and P_{ext} are determined by passive wall behavior. Like other soft tubes, blood vessels can be passively stretched by internal hydrostatic pressure exhibiting either linear or nonlinear $A(P)$ behavior. The behavior can be passive because the smooth muscle cells in the vessel wall are not activated. In experiments, on the other hand, the tube laws (Fig. 2a) are

usually obtained *in vitro* on the blood vessel segments. In that case, the activation can be performed by electrical, chemical or mechanical stimuli at certain experimental conditions.

The active response of the blood vessel to the hydrostatic pressure and flow shear rate includes coordinated changes in the lumen area and wall thickness and rigidity. *In vivo* arteries demonstrate active behavior responding to increased blood pressure by decreasing the lumen's area; the so-called Bayliss myogenic response [37], which is an active reaction of some smooth muscle cell types to stretch. The myogenic response of the smooth muscle cells to the shear stress at the wall is aimed at maintaining the volumetric flow rate. Increased/decreased wall shear stress evokes mechano-sensory reaction resulting in the smooth muscles relaxation/contraction accordingly. Muscle contraction leads to increase in the wall thickness and rigidity and decrease in the lumen, while muscle relaxation produces opposite effects.

The active response of the wall influences the $P_{tm}(A)$ curve, and *in vivo* for the active blood vessels, the S-shape and N-shape curves (Fig. 2b) can be obtained [38]. The S-shape curve is characterized by ambiguous dependence Ptm (A) (curve 2), while the N-shape curve by ambiguous dependence A (Ptm) (curve 3) in comparison with unambiguous relationship for the passive wall (curve 1). When the declining part exists in the Ptm (A) dependence, the flow through the vessel may be unstable [38]. The smooth muscles being involved in at least two types of response to the blood pressure and wall shear stress, what may result in a complex reaction. Consequently, in the tube law $P - P_{ext} = \Theta(A)$ for an active vessel, the function Θ may depend on the shear rate, pressure, concentrations of vasoactive chemicals and some other parameters involved in the myogenic reaction. The model of a blood vessel with the bioactive wall is developed in [38–40] and the nonlinear models for the S-type and N-type vessels are proposed in [41].

Experimentally measured pressure-flow relationships $\delta P(Q)$ for the passive blood vessels [27] are N-shaped and composed by two branches (branches I and III in Fig. 1b) with different positive slopes and a branch with negative slope (branch II in Fig. 1b). The collapsed state of the tube at different points are depicted in Fig. 1a. Gradual increase in the pressure drop δP starting from the fully collapsed state leads to partial opening of the vessel and growth of the volumetric rate (branch I). The vessel resistivity $Z = \delta P / Q$ is high and gradually increases with lumen opening, while the tube remains collapsed along its full length. Further increase in the pressure drop (branch II) leads to formation of the collapsed neck close to the inlet. The tube resistivity becomes high due to the flow separation, formation of the turbulent jet and high viscous dissipation [28]. The neck moves towards the outlet of the tube with subsequent increase in δP and al finally disappears. Then along branch III the tube is fully open and the

pressure-flow relationship is again determined by the tube resistivity which is much bigger than it was along the branch I.

One-dimensional models cannot describe the geometry of a collapsed tube, and the two-dimensional models are more successful for that purpose [1, 28, 42]. The two-dimensional flow in a rigid channel with a membrane insertion has been studied in [31, 43, 44].

A frequently cited two-dimensional model proposed in [49] includes Navier–Stokes equations for an incompressible fluid

$$(3.11) \qquad \operatorname{div}(\mathbf{v}) = 0, \qquad \rho_f \left(\frac{\partial \mathbf{v}}{\partial t} + (\mathbf{v}, \nabla) \mathbf{v} \right) = -\nabla p + \mu_f \Delta \mathbf{v},$$

and the momentum equation for the collapsible part of the wall

$$(3.12) \qquad \rho \frac{\partial^2 u_y}{\partial t^2} = \kappa T - \sigma_n - P_{ext}.$$

The boundary conditions are presented by the input parabolic flow

$$(3.13) \qquad x = 0: \quad v_x = \frac{4 v_{max}}{H^2} (H - y) y, \quad v_y = 0,$$

no-slip conditions at the rigid wall

$$(3.14) \qquad (0 \le x \le L, y = 0) \cup (0 \le x \le L_1, y = H)$$
$$\cup (L_1 + L_2 \le x \le L, y = H): \quad v_x = 0, \ v_y = 0$$

and stress and flow continuity conditions at the moving collapsible insertion

$$(3.15) \qquad (L_1 \le x \le L_1 + L_2, y = h(t, x)): \quad \mathbf{v} = \frac{\partial \mathbf{u}}{\partial t}, \quad \sigma_\tau = -\frac{\partial T}{\partial s},$$
$$\sigma_n = P_{ext} - T h_x''(1 + (h_x')^2)^{-3/2},$$

where $|AB| = L$, $|CD| = L_1$, $|EF| = L_3$, $L_2 = L - L_1 - L_3$, T and $\kappa = \partial \phi / \partial s$ are respectively membrane's tension and curvature, s is the coordinate measured along the membrane, ϕ is the angle between the tangent to the membrane and the axis of the tube, $\rho = \rho_s / \rho_f$, ρ_s is the density of the membrane, μ_f is the fluid viscosity, and σ_n and σ_τ are respectively normal and tangential stress in the membrane.

4. Linear stability analysis of collapsible tubes

A numerical method has been used in [57, 62] to study the spatio-temporal stability of the coupled fluid–thick collapsible tube. It is found that the system is subjected to both axisymmetric and azimuthal, unstable modes. The authors

determined whether a particular instability mode is convective or absolute using spatiotemporal stability analysis. For axisymmetric disturbances corresponding to the azimuthal wavenumber $n = 0$, they identified two convective instability modes, one propagating upstream and the other downstream.

For each of the non-axisymmetric disturbances $n = 1, \ldots, 10$, there are one mode representing absolute instability and one representing convective instability. Some of them are upstream propagating waves and some others are downstream propagating waves. The mode with azimuthal wavenumber $n = 1$ is shown to have the highest temporal amplification rate. When the steady state of the system takes the form of a divergent–convergent tube, the unstable modes occur only in the divergent part of the tube. In the convergent part, all the modes become stable regardless whether the tube takes the form of inflated or deflated tube.

Among the absolute unstable modes, there are three modes that have a frequency ratio in their cusp points [62] in good qualitative agreement with the observed experimental ratio frequency of unstable modes found by [10, 12, 13]. The energy transfer from the flow to the viscoelastic tube has been examined in [58, 60, 61]. It has been shown that when the tube is elastic, the energy transfer toward the wall from the fluid coincides with the instability of the system, as could be expected. When the tube is viscoelastic, however, there is a significant gap between the energy transfer toward the wall and the instability of the system due to kinetic energy dissipation in the wall. Based on linear stability analysis, the flow through collapsible tubes has been analyzed for the case of collapse's onset that induces self-excited oscillations [83]. The experimental data in the form of measured oscillation frequency at the onset of collapse of an elastic tube, is supplied as a base input parameter for the theoretical approximations in order to estimate the unmeasured parameters, such as critical oscillation speed, speed index, and tube cross-sectional area at collapse's onset. Some agreement between the theoretical and experimental results has been reported [83].

5. Linear and nonlinear dynamics in membrane channels

Two-dimensional models obviously avoid some of the complexities associated with the three-dimensional formulation. Solution of the two-dimensional problem has been obtained using the finite-element method (FEM) at different boundary conditions [42–48]. It has been found that the system admits two different steady solutions for the same system parameters, namely, Reynolds number, membrane tension, and geometrical parameters. This finding is consistent with the well-known feature of multiple solutions of the Navier–Stokes equations.

The primary difference between the observed steady solutions is that the system delivers different flows under the same conditions. This is similar to the

flow-limitation phenomena observed in collapsible tubes. Linear stability analysis of the two steady solutions has been carried out. It is found that both solutions are unstable, and the system goes back and forth from one steady solution to the other, in agreement with the numerical simulations in [44].

Detailed computations do not indicate an unambiguous correlation between flow limitation and self-excited oscillations of the membrane. When Q is confined, both stable and unstable regimes are realized. Instability of the parabolic steady inflow can be developed for certain values of the membrane's parameters. Steady state is observed when a membrane is inverted and flow limitation is not reached yet. In this case, a solution of the two-dimensional problem exhibits a set of interacting unstable modes [1, 5, 42–44]. This problem has been revisited more recently [69–77].

The interaction between the flow and a stretched-membrane channel for large membrane tension, large Reynolds number and long channel, has been studied in [69]. It is found that the primary mechanism of instability described by linear analysis is preserved when the amplitudes of the oscillations become large, even though the flow has been complicated substantially by the generation of secondary instabilities. A similar conclusion has been drawn in [57, 62] for a thick-walled tube. The computed frequency ratio of absolute unstable modes at their cusp point, where the frequency has the most important contribution to the physical wave, is in good agreement with experimental results [12].

For a membrane with large tension, it is found that a rich variety of different secondary instabilities are particularly evident upstream of the membrane, when the upstream-directed flux due to the oscillations has a magnitude close to that of the imposed mean flow. This conclusion suggests that there are some unstable upstream propagating waves in the system, as has been demonstrated in [57].

A careful inspection of Fig. 12 in [69] shows that the instability occurs in the divergent part of the channel, in qualitative agreement with the thick-tube analysis presented in [57]. Moreover, the same figure indicates that the unstable mode grows locally, which suggests that the instability of those modes is absolute, consistent with the results published in [57]. Though the geometries are different in the studies presented in [57] and [69], the dynamics in the two cases is surprisingly similar.

An unstable axisymmetric equilibrium state surrounded by two topologically equivalent stable non-axisymmetric states has been suggested in [70] as a possible explanation for the oscillations of collapsible tubes. The oscillations are classified as type I and type II. Type II occurs when the wall approaches its non-axisymmetric equilibrium shape.

The system's overall energy budget has been investigated in [71] to establish the critical Reynolds number at which the wall begins to extract energy from the flow. It is concluded that self-sustained oscillations occur when there is no more

energy transfer between the wall and the flow. This of course is only valid when the wall is elastic, as it has been demonstrated in [57, 60, 61]. The shape of the tube found in [71] indicates that the unstable mode with azimuthal wavenumber $n = 1$ is the dominant mode, as is confirmed in [57, 62].

Numerical simulations to explore the development of flow-induced self-excited oscillations in three-dimensional collapsible tubes is found in [74–76]. The simulations show that self-excited oscillations tend to arise preferentially from steady equilibrium configurations in which the tube is buckled non-axisymmetrically. The linear stability analysis of the flow interacting with a thick collapsible tube performed in [62] leads to the conclusion that the oscillations must be dominated by three non-axisymmetric modes with azimuthal wavenumbers $n = 1$, $n = 3$ and $n = 4$. Linear analysis of the coupling between Poiseuille flow and a tensioned membrane of finite length, using an eigenvalue approach to study the effect of wall-to-fluid mass ratio, is considered in [80].

6. Flow in thick collapsible tubes

The complete three-dimensional problem formulation includes the Navier–Stokes equations for the liquid, large-displacement momentum equations for the solid wall, constitutive relations for the wall material, and boundary conditions at the fluid–solid interface and the outer surface of the wall. Solutions of such complex problem can only be obtained numerically. The calculations are computer intensive because a tube that collapses is non-axisymmetric. On the other hand, it has been shown that a one-dimensional flow model combined with shell approximation for the wall gives a solution that is in reasonably good agreement with physiological data for blood's flow rate and pressure distribution in arteries. The reason is that P_{tm} typically remains positive and the arteries remain non-collapsed during the entire heart cycle [28].

A three-dimensional computer model has been developed to simulate fluid flow through a collapsible tube in [77]. It is found that the collapse is generally localized near the downstream end of the tube. Under certain conditions, however, it is also possible for the collapse to occur at multiple discrete locations separated by regions of open cross-section. A numerical method using generalized finite differences has been introduced in [78, 79] to solve for the unsteady viscous flow in collapsible tubes, simulating blood flow in stenotic carotid arteries. The Navier–Stokes equations have been used as the governing equations for the fluid. The tube wall has been treated as a free moving boundary whose elastic properties (the tube law) have been determined experimentally. Longitudinal tension has been included in the tube law. Physiologically-relevant pressure conditions and parameters have been used in the simulations. It is found that severe stenoses cause cyclic pressure changes between positive and negative values at

the throat of the stenosis, cyclic tube compressions and expansions, and shear stress changing directions in the region, just distal to the stenosis under unsteady conditions. It is concluded that those critical mechanical conditions may be related to excessive artery fatigue and possible rupture of the plaque cap.

A fluid–beam model, to overcome potential shortcomings of fluid–membrane models in collapsible channels, has been proposed in [46]. A finite-element code has been developed to solve the coupled nonlinear fluid–structure interaction equations, and a moving mesh with rotating spines has been used to enable a movable boundary. It is found that fluid–beam model compares favorably with those of the fluid–membrane model for very small wall stiffness. However, different results have been obtained in a thick-wall collapsible tube corresponding to real physiological application. The authors conclude that a thick-walled model provides a more realistic description of flow in collapsible channels.

A numerical method to solve the fluid-structure interaction in three-dimensional pulmonary arterial bifurcation with collapsible tubes has been proposed in [48]. A finite-element code has been used to calculate the nonlinear deformation of the thin-wall structure, and a commercial CFD solver is used to resolve the fluid flow. It is found that a large deformation of the structure significantly alters the flow field, while the fluid pressure strongly affects the deformation of the structure. In the bifurcation branches, the relatively short tube collapses into wavenumber mode. The strong collapse of the tube leads to a large contraction of the cross-sectional area and an increase in the resistance to the fluid flow. Recirculation occurs both upstream and downstream of the collapsed region of the tube.

The problem of finite axisymmetric deformation of a thick-walled elastic tube with circular cross-section subject to pressure on its external lateral boundaries and zero displacement at its ends has been formulated for an incompressible isotropic neo-Hookean material in [82]. It found that short tubes exhibit "corner bulging", and longer tubes exhibit multiple modes of deformation.

7. Structure and mechanical properties of blood vessels in normalcy and pathology

Blood vessel walls are composed of three layers, as depicted in Fig. 3a. Each layer has different thicknesses and viscoelastic properties [50–52]. The innermost layer is called intima and is composed of a monolayer of endothelium cells and the subendothelial layer reinforced by the collagen microfibres [53]. Endotheliocytes play an important role providing hemocompatibility and the mechano-sensory function that regulates the shear stress at the wall by influencing the vessel's lumen. In certain pathology such as hypertension, atherosclerosis and hyperlipemia, the thickness of the intima increases and its material parameters alter

a)   b)
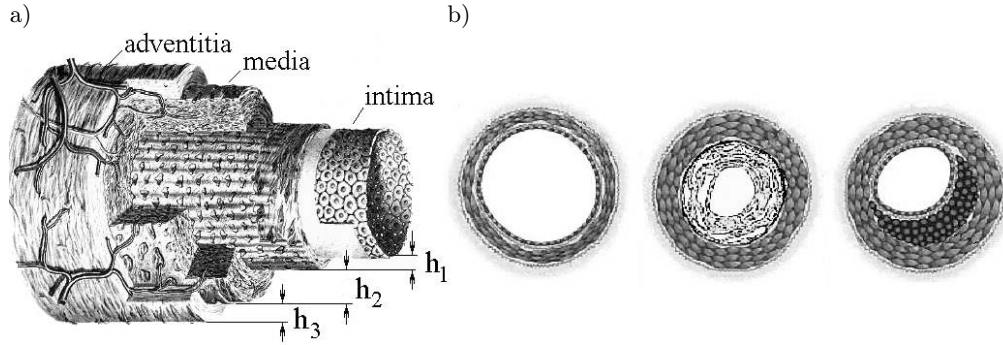
Fig. 3. a) Three layers of arterial wall. b) Cross-section in normalcy and certain pathology.

significantly due to fat accumulation, tissue development (intimal fibromuscular hypertrophy) or wall calcification [54,55]. This abnormality is depicted in Fig. 3b.

The middle layer is called media and is mechanically active. It consists of smooth muscle cells arranged in two helically distributed families, with a small pitch and very little dispersion in their orientation [53]. The thickness and elasticity of the media depend on the artery's type (elastic, muscular, or intermediate) and the smooth muscle tone. At elevated blood pressures, the activity of smooth muscle cell contributes significantly to the stiffness of the vessel's wall [56].

The outermost layer is called adventitia and is reinforced by two families of collagen fibers exhibiting some dispersion. Helical orientation of the fibers provides anisotropic properties of the adventitia, which differ from the properties of the media [51,53]. The adventitia influences the wall's mechanical properties mainly by facilitating tethering of the vessel to the surrounding tissues and by limiting the increase of the lumen's thickness at high arterial blood pressures. Relative thickness of the adventitia depends on the type and caliber of the blood vessel.

A brief review of recent measurements of structure and material parameters of blood vessel's walls is presented in [63]. It is important to note that different vascular pathology can be modeled by conjoined variations of the elasticity, Poisson's ratio, viscosity, density and thickness of the separate layers. Using the data summarized in [63], the three-dimensional problem of blood flow in arteries and veins can be modeled as a viscous flow in a multilayer viscoelastic tube, as discussed in the following section.

8. Fluid flow in multilayered distensible tubes

The stability of a viscous, incompressible, Poiseuille flow in a multilayered, thick-walled, viscoelastic tube has been studied in [63–65]. The pipe is composed of three anisotropic layers with thicknesses h_1, h_2 and h_3, where the total thick-

ness of the wall is $h = h_1 + h_2 + h_3$. The conservation equations for the fluid side are the incompressible Navier–Stokes equations

$$\nabla \cdot \mathbf{v} = 0,$$

(8.1)
$$\frac{\partial \mathbf{v}}{\partial t} + \mathbf{v} \cdot \nabla \mathbf{v} = -\frac{1}{\rho_f} \nabla p + \frac{1}{\rho_f} \nabla \cdot \hat{\sigma},$$

$$\nabla \cdot \mathbf{u}^j = 0,$$

(8.2)
$$\rho_w^j \frac{\partial^2 \mathbf{u}^j}{\partial t^2} = -\nabla p^j + \nabla \cdot \hat{\sigma}^{\mathbf{j}},$$

where $\mathbf{v}$ is the flow velocity, $\mathbf{u}^j$ is the displacement of the wall layers $j = 1, 2, 3$, and ρ_f, p, $\hat{\sigma}$ and ρ_w^j, p^j, $\hat{\sigma}^j$ are, respectively, the density, hydrostatic pressure and stress tensor for the fluid and the wall layers.

A viscoelastic Kelvin–Voight material has been considered for the solid

$$\kappa^j \frac{\partial}{\partial t} \boldsymbol{\sigma}_i^j + \boldsymbol{\sigma}_i^j = A_{ik}^j \boldsymbol{\varepsilon}_k^j + \mu_w^j \frac{\partial}{\partial t} \boldsymbol{\varepsilon}_i^j,$$

(8.3)
$$\hat{\varepsilon}^j = \frac{1}{2}(\nabla \mathbf{u}^j + \nabla \mathbf{u}^{jT}),$$

where $\boldsymbol{\sigma}$ and $\boldsymbol{\varepsilon}$ are the stress and strain vectors, A_{ik}^j is the matrix of elasticity coefficients, μ_w^j are the layers' viscosities, and κ^j is the stress relaxation time for each of the three layers.

The boundary conditions include the continuity conditions for the fluid velocity and displacement of the inner layer, and for the normal and tangential stresses at the fluid–solid interface, as well as the continuity conditions for the displacements and stresses at the two interfaces between the three solid layers:

(8.4)
$$r = R : \quad \mathbf{v} = \frac{\partial \mathbf{u}^1}{\partial t}, \quad \hat{\boldsymbol{\sigma}}_n^1 = \hat{\boldsymbol{\sigma}}_n, \quad \hat{\boldsymbol{\sigma}}_\tau^1 = \hat{\boldsymbol{\sigma}}_\tau,$$

(8.5)
$$r = R + h_1 : \quad \mathbf{u}^1 = \mathbf{u}^2, \quad \hat{\boldsymbol{\sigma}}_n^1 = \hat{\boldsymbol{\sigma}}_n^2, \quad \hat{\boldsymbol{\sigma}}_\tau^1 = \hat{\boldsymbol{\sigma}}_\tau^2,$$

(8.6)
$$r = R + h_1 + h_2 : \quad \mathbf{u}^2 = \mathbf{u}^3, \quad \hat{\boldsymbol{\sigma}}_n^2 = \hat{\boldsymbol{\sigma}}_n^3, \quad \hat{\boldsymbol{\sigma}}_\tau^2 = \hat{\boldsymbol{\sigma}}_\tau^3.$$

Finally, at the outer surface of the tube either a no-stress boundary condition [66]:

(8.7)
$$r = R + h : \quad \hat{\boldsymbol{\sigma}}_n^3 = 0, \quad \hat{\boldsymbol{\sigma}}_\tau^3 = 0$$

or a no-displacement boundary condition is applied [63]:

(8.8)
$$r = R + h : \quad \mathbf{u}^3 = 0,$$

where the subscripts n and τ respectively denote the normal and tangential components of the stress tensor.

Solution of the linearized fluid–structure interaction problem has been found as a superposition of the unperturbed steady-state liquid flow and small disturbances in the form of normal modes

(8.9)
$$(\mathbf{v}, p) = (\mathbf{v}^*, p^*) + (\tilde{\mathbf{v}}, \tilde{p})e^{st+ikz+in\theta},$$
$$(\mathbf{u}^j, p^j) = (\mathbf{u}^{*j}, p^{*j}) + (\tilde{\mathbf{u}}^j, \tilde{p}^j)e^{st+ikz+in\theta},$$

where $\tilde{\mathbf{v}}$, $\tilde{\mathbf{u}}^j$, $\tilde{p}$ and $\tilde{p}^j$ are the amplitudes of the corresponding disturbances, $k = k_r + ik_i$, $s = s_r + is_i$, k_r is the wavenumber, k_i and s_r are spatial and temporal amplification rates, and s_i is the wave frequency. The steady part $(\mathbf{v}^*, p^*)$ of (8.9) is identified with the Poiseuille flow. Both isotropic and transversely isotropic materials for the wall layers have been studied.

According to the experimental data summarized in [32], the plane of isotropy of each layer is perpendicular to the radial axis, and the matrix of elasticity coefficients is

$$(A_{ik}^j)^{-1} = \begin{pmatrix} \dfrac{1}{E_2^j} & \dfrac{-\nu_2^j}{E_2^j} & \dfrac{-\nu_2^j}{E_2^j} & 0 & 0 & 0 \\[2mm] \dfrac{-\nu_2^j}{E_2^j} & \dfrac{1}{E_1^j} & \dfrac{-\nu_1^j}{E_1^j} & 0 & 0 & 0 \\[2mm] \dfrac{-\nu_2^j}{E_2^j} & \dfrac{-\nu_1^j}{E_1^j} & \dfrac{1}{E_1^j} & 0 & 0 & 0 \\[2mm] 0 & 0 & 0 & \dfrac{1}{G_2^j} & 0 & 0 \\[2mm] 0 & 0 & 0 & 0 & \dfrac{1}{G_1^j} & 0 \\[2mm] 0 & 0 & 0 & 0 & 0 & \dfrac{1}{G_1^j} \end{pmatrix},$$

where G_2^j are the shear moduli, $E_{1,2}^j$ are the Young's moduli, and $\nu_{1,2}^j$ are the Poisson's ratios of the layers. The values of $E_{1,2}^j$, $G_{1,2}^j$ and $\nu_{1,2}^j$ are different for different blood vessels (elastic or muscle type) and for healthy vessel walls and those for certain pathological conditions including hypertension, atherosclerosis and hyperlipidemia.

The temporal and spatial eigenvalues of the system have been computed using the numerical technique described in [64, 65]. The above fluid–structure interaction problem has a large number of parameters, and effects of Reynolds number, viscous and elastic parameters and thicknesses of the wall layers on

the system stability have been thoroughly studied. See Appendices I and II for, respectively, the difference between temporal and spatial instabilities and the numerical method used to compute them.

The temporal and spatial eigenvalues of the system have been computed for the no-displacement (Fig. 4) and the no-stress (Fig. 5) boundary conditions at the outer surface of the vessel's wall. The modes located near the real axis in the complex (s_r, s_i)-plane are solid-based, and those located near the imaginary axis are fluid-based. The modes near the origin efficiently couple the solid and fluid motions. For a cylindrical water column with free boundaries, the fluid-based modes remain only in the (s_r, s_i)-plane, whereas for an empty viscoelastic shell, the fluid-based modes disappear and only solid-based modes could be identified. The modes involved efficiently in the fluid–solid interaction are placed near the origin of the complex plane where unstable modes with $s_r > 0$ are located. As can
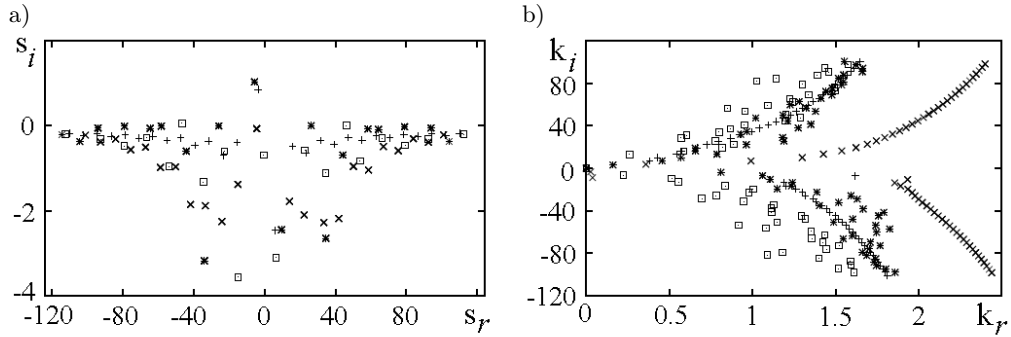
Fig. 4. No-displacement boundary condition at the outer surface of a fluid-filled tube, computed at Re = 10, $\mu_r^j = 0$, $h = 0.4$, $h_1 = 0.14$, $h_2 = h_3 = 0.63$, $\rho_r^j = 1$, $E^j = 2G^j$; a) temporal eigenvalues, b) spatial eigenvalues. +: isotropic wall material $G^j = 1$; □: $G^1 = G^2 = 1, G^3 = 20$; *: $G^1 = G^3 = 1, G^2 = 20$; ×: $G^2 = G^3 = 1, G^1 = 20$.
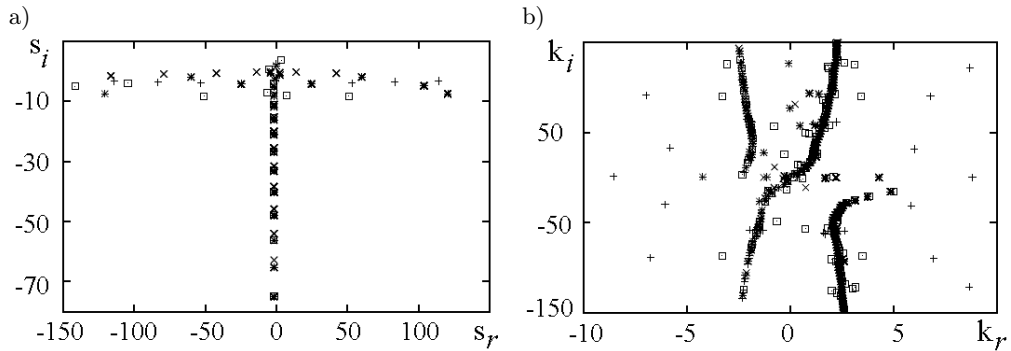
Fig. 5. No-stress boundary condition at the outer surface of a fluid-filled tube, computed for isotropic and anisotropic walls; a) temporal eigenvalues, b) spatial eigenvalues. Parameters and symbols are the same as in Fig. 4.

be seen in Fig. 4a for the no-displacement condition, the modes are mostly solid-based, because the fixed wall determines the fluid motion and wave propagation. For the free unloaded wall, the modes are mostly fluid-based as depicted in Fig. 5a. In this case, the wall motion is strongly determined by the fluid flow.

Unless indicated otherwise, the numerical values of the dimensionless physical parameters are as follows: wavenumber $k_r = 2.5$; frequency $s_i = 2$; Reynolds number $\mathrm{Re} = 100$; ratio of fluid inertia to elastic forces $\Gamma = 1$; Young's modulus Ξ and shear modulus Θ are $\frac{1}{3}\Xi_1^j = \frac{1}{3}\Xi_2^j = \Theta_2^j = \Theta_1^j = 1$; solid-to-fluid density ratio $\rho^j = 1$; viscosity of the solid $\mu_w^j = 0$; tube radius $R = 1$; and layer thickness $h = 0.1$, $h_1 = 0.02$, $h_2 = 0.02$, $h_3 = 0.06$. The calculated results have been found to be practically insensitive to the Poisson's ratio of the layers.

The spectrum in the complex wavenumber plane (k_r, k_i) forms the branches in the upper part $(k_i > 0)$ and in the lower part $(k_i < 0)$ of the (k_r, k_i)-plane. The modes in the upper part are the monochromatic components of the solution for $z > 0$, i.e. in the region located downstream the source of perturbations. The modes in the lower part of the (k_r, k_i)-plane correspond to the solutions located upstream of the source. At any given cross-section of the tube, superposition of the forward and backward propagating waves produces a complicated pattern of pressure and flow time variations in the fluid and wall oscillations. The pressure and flow distributions depend on the fastening conditions at the wall, because the spectrum differs for the no-displacement (Fig. 4b) and no-stress (Fig. 5b) boundary conditions. The spatial amplification rate increases with wavenumber at both boundary conditions [64–66].

As has been shown through the extensive numerical computations in [63–66], the fluid–structure system can be stabilized by a proper choice of shear moduli and viscosities of the separate layers for different material parameters, Re and Γ values, and boundary conditions. This enables the suppression of absolute instabilities and prevention of self-excited oscillations and noise generation. The dependence of the temporal amplification rate of the most unstable mode on the shear modulus of one of the layers, while the shear moduli of the other two layers remain unchanged is plotted in Fig. 6a for the no-stress boundary condition.

In the considered variation range of Θ_1^j and Θ_2^j, one can see that an increase in the shear modulus of the three layers simultaneously leads to an increase in the amplification rate, what is indicated by the solid line in Fig. 6a. An increase in the shear modulus $G_1^1 = G_2^1$ of the inner layer which is in contact with the fluid, while the shear moduli of the other two layers are fixed at $\Theta_1^2 = \Theta_1^3 = \Theta_2^2 = \Theta_2^3 = 1$, leads to noticeable decrease in the temporal amplification rate down to its negative values $s_r < 0$, which corresponds to a temporal stability of the system, what is indicated by curve 2 in Fig. 6a. At sufficiently large values ($\Theta_1^1 = \Theta_2^1 \geq 7$ in Fig. 6a), the system becomes stable. An increase in the shear modulus $\Theta_1^2 = \Theta_2^2$

a)

b)
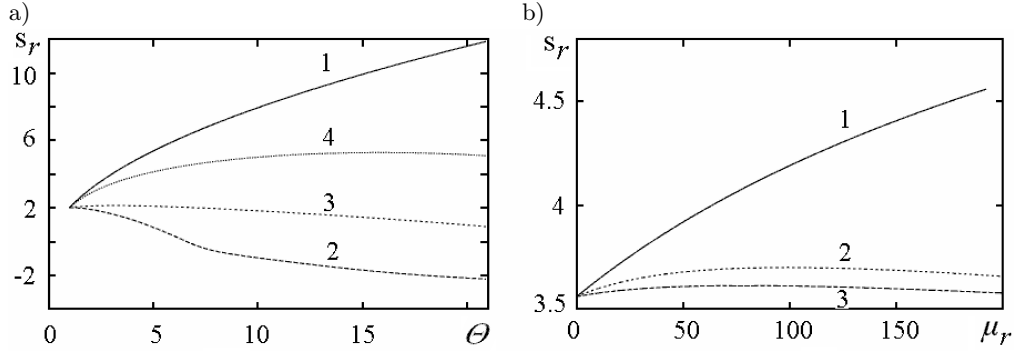
Fig. 6. a) Temporal amplification rate versus shear modulus Θ for viscoelastic layers, $\mu_r^1 = \mu_r^2 = \mu_r^3 = 30$. Isotropic walls, $\Theta_1^1 = \Theta_1^2 = \Theta_1^3 = \Theta$ (curve 1); non-isotropic walls, $\Theta_1^2 = \Theta_1^3 = 1$, $\Theta_1^1 = \Theta$ (curve 2); $\Theta_1^1 = \Theta_1^3 = 1$, $\Theta_1^2 = \Theta$ (curve 3); $\Theta_1^1 = \Theta_1^2 = 1$, $\Theta_1^3 = \Theta$ (curve 4). b) Temporal amplification rate of the most unstable mode versus the viscosity of one of the three isotropic layers, $\Theta_1^1 = \Theta_1^2 = \Theta_1^3 = 1$. Layer viscosities are $\mu_r^2 = \mu_r^3 = 0$ (curve 1); $\mu_r^1 = \mu_r^3 = 0$ (curve 2); $\mu_r^1 = \mu_r^2 = 0$ (curve 3).

or $\Theta_1^3 = \Theta_2^3$, while the parameters of other layers are fixed $\Theta_1^{1,3} = \Theta_2^{1,3} = 1$ or $\Theta_1^{1,2} = \Theta_2^{1,2} = 1$, stabilizes the system as is indicated by curves 3–4 in Fig. 6a. The obtained results correspond to experimental and theoretical considerations of flow instability over compliant surfaces. The results presented in Fig. 6a reveal that flow stabilization in the pliable tube can be achieved by using a relatively rigid inner coating (inner layer) of certain thickness. These results are consistent with the conclusions made for a two-layer, anisotropic Kramer-type coating, which was found to be important for flow stabilization [67, 68].

The dependence of the temporal amplification rate on the viscosity of one of the layer, while the other two layers are considered elastic (i.e. non-viscous), is plotted in Fig. 6b for the no-stress boundary conditions. An increase in the viscosity of the second and third layers results in insignificant variation of the amplification rate, although the instability mode is slightly damped for a very viscous wall material. Increasing the viscosity of the first layer that is in contact with the fluid significantly destabilizes the system. In other words, high viscosity of the first layer enhances the fluid–structure interaction and, consequently, the energy transfer from the fluid to the solid, producing the system instability.

For the viscoelastic layers, as distinct from the elastic wall case, an increase in the shear modulus $\Theta_1^3 = \Theta_2^3$ of the outer layer leads to increasing the system instability. On the other hand, a stabilizing effect of the shear modulus of the inner layer is observed at sufficiently high values $\Theta_1^1 = \Theta_2^1$. The system stability and the behavior of the unstable modes are very sensitive to the material parameters of the layers, as it has been found by numerical computations within a wide range of thicknesses and viscoelastic parameters of the layers. The sta-

bilizing effect of rigidity of the inner layer has been observed in each case at $\Theta_1^1 = \Theta_2^1 \geq \Theta^*$, where the value Θ^* depends on the viscosity of the layer.

Influence of the shear modulus and Young's modulus on the most unstable mode at the no-displacement boundary conditions, is illustrated by Fig. 7a. As the depicted results were obtained for a variety of material parameters, the most unstable mode remains unstable for all the considered ranges of shear moduli. Increasing the shear modulus of any single layer does not stabilize the system. However, increasing both the shear and Young's modules has a non-uniform effect on the temporal amplification rate. Variation of the shear modulus of the middle layer G^2 and Young's moduli E_1^2 and E_2^2, while fixing $E_2^2 = 2G^1$, $E_1^2 = 2G^2$, causes an opposite effect as compared to varying the shear modulus of the first layer G^1. Note that higher values of the amplification rate have been obtained by variation of the shear modulus G^2 of the second layer, as compared to the values obtained by varying the shear modulus G^1 of the first layer (Fig. 7a). Increasing the shear modulus G^3 of the third layer, while $E_2^3 = 2G^3$, $E_1^3 = 2G^3$, leads to a relatively large decrease in the amplification rate of the most unstable mode.
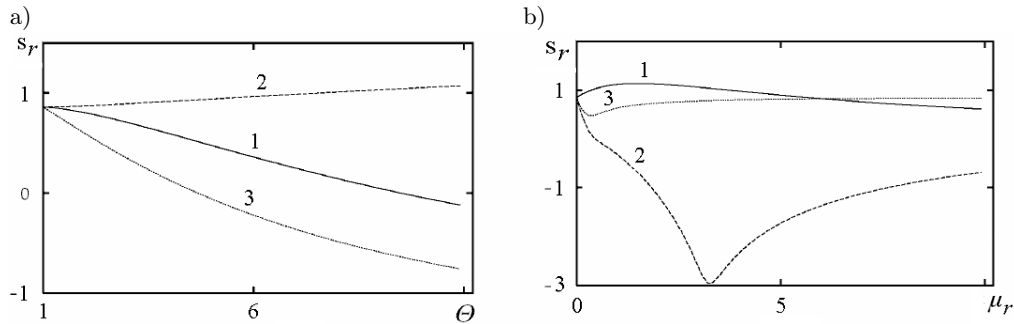
Fig. 7. a) Amplification rate of the most unstable mode versus dimensionless shear modulus of one of the layers, $j = 1, 2, 3$ (curves 1–3). b) Amplification rate of the most unstable mode versus dimensionless viscosity of one of the layers, $j = 1, 2, 3$ (curves 1–3); $h = 0.4$, $h_1 = 0.04$, $h_2 = 0.18$, $h_3 = 0.18$.

Dependence of the amplification rate of the most unstable mode on the viscosity of each of the layers is plotted in Fig. 7b. In each case, the viscosities of two layers are kept constant while the viscosity of the remaining layer varies. It is clear that increasing the viscosity of the inner layer, which is in contact with the fluid, leads to some increase in the positive amplification rate (curve 1 in Fig. 7b). The effect can be explained by better fluid–solid coupling when the viscosity of the inner layer is sufficiently high. The viscosity of the middle layer produces a stabilizing effect, while the viscosity of the outer layer does not influence the system stability. As a result of these findings, a 'successful' wall material can be proposed as a sandwich formed by a high-damping viscoelastic layer placed between two low-damping layers. Since the system sta-

bilization is determined by the energy transfer at the fluid–wall interface, the successful wall materials possess needed properties for energy transferd and absorption.

Influence of anisotropy of the layers on the system stability has been studied by computing the temporal amplification rate of the most unstable mode for the isotropic layers $\Xi_1^j = \Xi_2^j$, $j = 1, 2, 3$, when at least one of the layers is transversely isotropic and $\Xi_1^j \neq \Xi_2^j$. Note that a wall composed of three isotropic layers with different viscoelastic parameters becomes anisotropic along the r-axis. Some numerical results illustrating the complex influence of wall anisotropy on the temporal and spatial spectra are presented in Fig. 8, for the no-stress boundary condition. Increasing the Young's modules of all three layers (Fig. 8a), of inner (Fig. 8b), middle (Fig. 8c) and outer (Fig. 8d) layer, is compared in each part of the figure for isotropic and anisotropic materials.

Curve 1 in Fig. 8a is obtained by varying the $\Xi_1^j = \Xi_2^j = \Xi$, $j = 1, 2, 3$, while the other parameters are held constant. We observe a dramatic fall of the temporal amplification rate, although the mode remains unstable. Increasing the
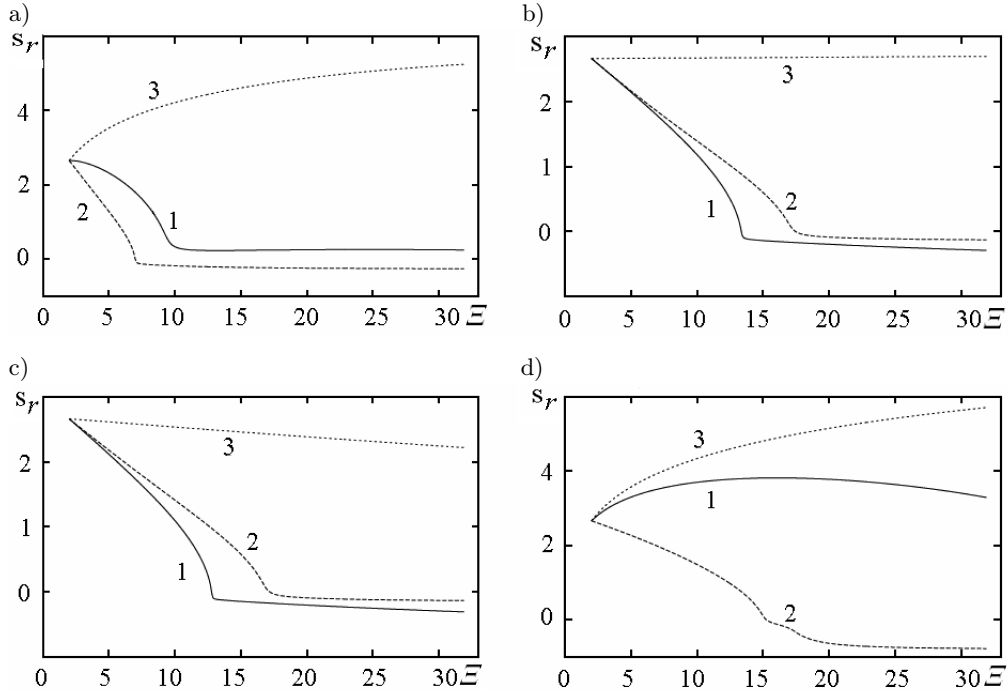
Fig. 8. Temporal amplification rate of the most unstable mode for anisotropic layers at different values of Young's modules. a) $\Xi_2^j = \Xi_1^j = \Xi$ (curve 1), $\Xi_1^j = \Xi$ (curve 2), $\Xi_2^j = \Xi$ (curve 3); b) $\Xi_2^1 = \Xi_1^1 = \Xi$ (curve 1), $\Xi_1^1 = \Xi$ (curve 2), $\Xi_2^1 = \Xi$ (curve 3); c) $\Xi_2^2 = \Xi_1^2 = \Xi$ (curve 1), $\Xi_1^2 = \Xi$ (curve 2), $\Xi_2^2 = \Xi$ (curve 3); d) $\Xi_2^3 = \Xi_1^3 = \Xi$ (curve 1), $\Xi_1^3 = \Xi$ (curve 2), $\Xi_2^3 = \Xi$ (curve 3).

parameters $\Xi_1^j = \Xi$, $j = 1, 2, 3$, leads to system stabilization, as seen in curve 2 in Fig. 8a, which is obtained by varying the parameter $\Xi_1^j = \Xi$, $j = 1, 2, 3$ while other parameters are held constant. When $\Xi \leq 8$, the most unstable mode becomes stable. Increasing the parameter $\Xi_2^j = \Xi$ for all the layers $j = 1, 2, 3$ leads to opposite effect and enhances the system instability.

Increasing of the Young's moduli $\Xi_{1,2}^j$ of the first, second and third layers separately, influences the system stability in different ways, as shown in Fig. 8b–d. The temporal amplification rate decreases noticeably with increasing $\Xi_1^1 = \Xi_2^1$ (curve 1 in Fig. 8b) and Ξ_1^1 (curve 2 in Fig. 8b), and the system becomes stable at $\Xi_1^1 \leq 13$ and $\Xi_1^1 \leq 18$. Increasing the value of Ξ_2^1 does not influence the stability of the most unstable mode.

Effect of Young's modulus of the second layer is similar to the effect of Young's modulus of the first layer, as can be concluded from Fig. 8c. Stabilization of the system can be reached at approximately the same values of $\Xi_1^2 \leq 13$ and $\Xi_1^2 \leq 18$ for the case $\Xi_1^2 = \Xi_2^2$ (curve 1 in Fig. 8c), and Ξ_1^2 (curve 2 in Fig. 8c).

Anisotropy of the third layer exerts the most significant influence, as shown in Fig. 8d. An increase in $\Xi_1^3 = \Xi$ stabilizes the system, while an increase in $\Xi_2^3 = \Xi$ destabilizes it. When $\Xi_1^3 = \Xi_2^3 = \Xi$, the system remains unstable and the temporal amplification rate is approximately of the same order of magnitude as the mean temporal amplification rate obtained by varying Ξ_1^3 and Ξ_2^3.

The present numerical results reveal some novel opportunities for stabilizing a fluid flow in transversely isotropic, multilayer, viscoelastic tubes, by proper choice of elastic and viscoelastic materials for the layers. In the blood vessels, differences in Ξ_1^j and Ξ_2^j are connected with wall structure. Each layer is composed of a set of sheets (laminae) with different material parameters, while connection between the sheets (in the radial direction) is provided by the fibers that may be more extensible and flexible than the fibers located in the sheets in the plane of isotropy of the layers. The difference is most important for the middle layer composed of several elastic laminae attached to each other by elastic fibers. In man-made materials, anisotropy is determined by orientation of the polymer chains, grains and other inclusions and by orientation of the fibers in fiber-reinforced composites and textiles.

9. Conclusions

A review of liquid and gas flows in compliant tubes, ducts and cavities in living bodies is presented. Additionally to briefly summarizing what is already in the open literature, the present paper also contains some new results never published before.

Biofluid flows in compliant ducts exhibit common features, caused by system instability, such as flow limitation, wall oscillations and noise generation. These physical phenomena are identified at certain geometry, flow regime and boundary conditions for blood flow in arteries and veins and through stents and grafts, in air flow in the airways (e.g., nasal cavities, larynx, glottis, and bronchial tree), in urine flow in the urethra, and in other biological flows. Wall oscillations and complex flow behavior, collapse of ducts and pressure-independent flow regimes are observed in the aforementioned biological conduits.

Noise generation is detected over some normal and pathological blood vessels, in the bronchial tree (dry and moist rales, coughing), in larynx (speech generation), and in glottis (snoring). Air flow during forced expiration is accompanied by wheezing, and registration of the generated sound and differentiation between dry and moist rales is important for diagnostics.

A proper model for observed physiological phenomena is the Starling resistor. The lumped parameter model as well as the one-dimensional, two-dimensional and three-dimensional models of fluid flow in rigid and compliant tubes in series, can be used for detailed investigations of the aforementioned phenomena and to provide biomechanical explanation of the registered pressure and flow curves and generated sounds. The choice depends on the desired details of the model and its consistency with measured data, which can be collected as time series or three-dimensional fluid flow and wall displacement distributions obtained, for example, by magnetic resonance imaging (MRI).

A model of blood vessel as a three-layer tube composed of viscoelastic anisotropic materials with different material parameters is useful for detailed investigation of the flow stability, wave propagation and reflection, and wall oscillations at different flow regimes. Stability analysis of steady flow reveals some reasonable strategies to increase the system stability by influencing the most unstable mode. It is shown that the system instability strongly depends on the rheological properties of the wall. The shear moduli and viscosities of the layers produce the strongest effect on the temporal and spatial amplification rates and the group velocity of the unstable modes. When a compliant tube is composed of three layers with the same material parameters, the system is found to be unstable. When the material parameters of the layers are different, the system may possess lower temporal amplification rates and even become stable.

An increase in the shear moduli of the inner and middle layers decreases the temporal amplification rate and stabilizes the system, whereas some increase in rigidity of the outer layer eliminates the temporal instability of the steady viscous flow in a compliant tube with no-stress boundary condition at the outer surface of the tube. Comparative analysis of the system stability at the no-displacement and no-stress boundary conditions at the outer surface of the duct reveals that

stabilization of the system can be attained by increasing the rigidity of the inner layer in both cases. For transversely isotropic material, temporal stability can be achieved by increasing the shear modulus in the plane of isotropy of any of the layers at the no-stress boundary condition, and by increasing the viscosity of the second layer at the no-displacement condition.

The numerical results herein reveal some novel opportunities to eliminate absolute instabilities and flow-induced wall vibrations by judicious choices of shear moduli and viscosities of individual layers. Therefore, optimal parameters of a composite wall that effect system stabilization, can be computed to construct efficient sound absorption and vibration damping coatings for aerospace vehicles and other noise-generating devices. As applied to biomedical problems, the present results shed new light on the stability/instability of blood flow in vessels pathologically changed by wall thickening and corresponding variations of viscosities, elastic coefficients and densities of the layers. Based on the presented theory, the results can be generalized for non-axisymmetric disturbances, which can exist in both blood vessels and tubes of technical applications.

Appendix I: Temporal and spatial instabilities

We give in this appendix a very brief refresher on the difference between temporal and spatial instabilities. When a physical problem is described by a linear set of partial differential equations, where the solution depends, for example, on time t and distance z, while the coefficients of the partial differential equations are independent of both t and z, a solution, $f(t, z)$ in the form of a normal mode could be sought, that is of the form

$$f(t, z) = h e^{st+ikz},$$

where h is in this case a constant and s and k are complex numbers, thus,

$$s = s_r + is_i, \qquad k = k_r + k_i.$$

The system is then said to be temporally unstable if $s_r > 0$. The analysis of spatial instability has to be handled with more care. In fact, the sign of k_i does not give a direct indication of the stability or instability of the system, in spite of the fact that the function f goes to infinity when z goes to $\pm\infty$ for, respectively, positive and negative k_i. The positive and negative signs of k_i indicate in general the presence of evanescent modes describing perturbations located upstream and downstream of the coordinate system's origin used in the problem formulation. The only mode that represents a spatial instability of the system is the one mode crossing the imaginary axis in the Fourier's contour

during the process of lowering the Laplace's contour. The lowering process of the Laplace's contour could proceed until it reaches the imaginary axis of the complex Laplace's plane, (s_r, s_i). The spatial instability is said to be convective, and is in this case equivalent to a temporal instability. When the process of lowering a Laplace's contour is prohibited by the coalescence of two modes coming from the opposite halves of the Fourier's contour, the instability is said to be an absolute one. There is no equivalence between the two kinds of instability.

Appendix II: Numerical method

A numerical procedure has been developed by the present authors to solve the linearized fluid and solid equations coupled via the boundary conditions. Solutions are sought in the form of normal modes in the azimuthal and axial direction, allowing the computation of s values for a given k wavenumber (temporal eigenvalues) and k values for a given s frequency (spatial eigenvalues). The numerical procedure for axisymmetric modes consists of finding two independent solutions, say X_1 and X_2, in the fluid medium satisfying the boundary condition at the tube axis. The component of the vectors X_1 and X_2 are the two velocity components, the first-order derivative of the axial velocity component with respect to r, and the pressure in the fluid medium. The independence of the two solutions is ensured by starting the computation with one of the two independent vectors formed by several values of X_1 and X_2, and can be obtained by starting the computations with the boundary conditions $X_1^0 = (1, 0, 0, 0)$ and $X_2^0 = (0, 0, 1, 0)$. With this choice, the boundary conditions at $r = 0$ are satisfied by both solutions X_1 and X_2 . It should be noted that to initiate the computation of X_1 and X_2, the chosen X_1^0 and X_2^0 must form a set of free vectors, which is sufficient for the computed X_1 and X_2 to be free vectors. Then the general solution in the fluid medium is an arbitrary combination of the free solutions, namely, $X = \alpha_1 X_1 + \alpha_2 X_2$, where α_1 and α_2 are arbitrary constants.

Similarly, for the displacement field in the solid layers, we solve the linearized equations for two independent solutions, say Y_1 and Y_2. The components of the vectors Y_1 and Y_2 are the two displacement components, the first-order derivative of the axial displacement component with respect to r, and the pressure in the wall layers. The solution for the solid layers is $Y = \beta_1 Y_1 + \beta_2 Y_2$, where β_1 and β_2 are arbitrary constants. The independence of the solutions is ensured by the foregoing procedure. The solutions satisfy the boundary conditions at the outer surface $r = R + h$. The boundary conditions at the interface $r = R$ lead to the eigenvalue problem $MC = 0$, where the elements of the matrix M are a linear combination of the particular solution components and their derivatives,

which involve all the rheological, geometric and hydrodynamic parameters of the system. The components of the vector C are the arbitrary constants α_1, α_2, β_1 and β_2. The characteristic equation is obtained by setting $\mathrm{Det}(M) = 0$. The numerical procedure used for solving the ODE equations is based on a fourth-order Runge–Kutta method [58]. An iterative technique using the steepest decent method is developed to find the double roots of the dispersion equation, namely $\mathrm{Det}(M) = 0$.

References

1. T.J. PEDLEY, X.Y. LUO, *Modelling flow and oscillations in collapsible tubes*, Theoretical and Computational Fluid Dynamics, **10**, 277–294, 1998.

2. T.J. PEDLEY, *Mathematical modeling of arterial fluid dynamics*, Journal Engineering Mathematics, **47**, 419–444, 2003.

3. M. HEIL, O.E. JENSEN, *Flows in deformable tubes and channels—Theoretical models and biological applications*, [in:] *Flow in Collapsible Tubes and Past Other Highly Compliant Boundaries*, T.J. PEDLEY, P.W. CARPENTER [Eds.], pp. 15–49, Kluwer, Dordrecht, The Netherlands, 2003.

4. V. KUMARAN, *Hydrodynamic stability of flow through compliant channels and tubes*, [in:] *Flow in Collapsible Tubes and Past Other Highly Compliant Boundaries*, T.J. PEDLEY, P.W. CARPENTER [Eds.], pp. 95–118, Kluwer, Dordrecht, The Netherlands, 2003.

5. J.B. GROTBERG, O.E. JENSEN, *Biofluid mechanics in flexible tubes*, Annual Review of Fluid Mechanics, **36**, 121–147, 2004.

6. J.C. GUNERATNE, T.J. PEDLEY, *High-Reynolds-number steady flow in a collapsible channel*, Journal of Fluid Mechanics, **569**, 151–184, 2006.

7. M. HEIL, A.L. HAZEL, *Fluid-Structure Interaction in Internal Physiological Flows*, Annual Review of Fluid Mechanics, **43**, 141–162, 2011.

8. T.J. PEDLEY, P.W. CARPENTER [Eds.], *Flow in Collapsible Tubes and Past Other Highly Compliant Boundaries*, Kluwer, Dordrecht, The Netherlands, 2003.

9. C.D. BERTRAM, *Experimental studies of collapsible tubes*, in *Flow in Collapsible Tubes and Past Other Highly Compliant Boundaries*, T.J. PEDLEY, P.W. CARPENTER [Eds.], pp. 51–65, Kluwer, Dordrecht, The Netherlands, 2003.

10. C.D. BERTRAM, J. TSCHERRY, *The onset of flow-rate limitation and flow-induced oscillations in collapsible tubes*, International Journal of Solids and Structures, **22**, 1029–1045, 2006.

11. F.P. KNOWLTON, E.H. STARLING, *The influence of variations in temperature and blood pressure on the performance of the isolated mammalian heart*, Journal of Physiology, **44**, 206–219, 1912.

12. C.D. BERTRAM, R.J. CASTLES, *Flow limitation in uniform thick-walled collapsible tubes*, International Journal of Solids and Structures, **13**, 399–418, 1999.

13. C.D. BERTRAM, T.J. PEDLEY, *A mathematical model of unsteady collapsible tube behaviour*, Journal of Biomechanics, **15**, 39–50, 1982.

14. C.D. Bertram, *Flow-induced oscillation of collapsed tubes and airway structures*, Respiratory Physiology and Neurobiology, **163**, 256–265, 2008.

15. M. Bonis, C. Ribreau, *Etude de quelques propriétés de l'écoulement dans une conduite collabable*, La Houille Blanche, **4**, 165–173, 1978.

16. N. Gavriely, T.R. Shee, D.W. Cugell, J.B. Grotberg, *Flutter in flow-limited collapsible tubes: a mechanism for generation of wheezes*, Journal of Applied Physiology, **66**, 2251–2261, 1989.

17. R.W. Brower, C. Scholten, *Experimental evidence on the mechanism for the instability of flow in collapsible vessels*, Medical Biological Engineering, **13**, 839–845, 1975.

18. D.J. Griffiths, *Urethral elasticity and micturition hydrodynamics in females*, Medical and Biological Engineering, **7**, 201–215, 1969.

19. D.J. Griffiths, *Hydrodynamics of male micturition*, Medical and Biological Engineering, **9**, 589–596, 1969.

20. J.B. Grotberg, N. Gavriely, *Flutter in collapsible tubes: a theoretical model of wheezes*, Journal of Applied Physiology, **66**, 2262–2273, 1989.

21. T. Yamane, T. Orita, *Self-excited oscillations with and without supercritical flow in collapsible tubes*, in *Proceedings of the 7th International Conference on Biomedical Engineering*, pp. 502–504, Singapore, 1992.

22. W.A. Conrad, M.L. Cohen, D.M. Mc Queen, *Note on the oscillations of collapsible tubes*, Medical and Biological Engineering and Computing, **16**, 211–214, 1978.

23. T.J. Pedley, B.S. Brook, R.S. Seymour, *Blood pressure and flow rate in the giraffe jugular vein*, Philosophical Transactions of Royal Society London, Ser. B, **351**, 855–866, 1996.

24. W.A. Conrad, *Pressure-flow relationships in collapsible tubes*, IEEE Transactions on Biomedical Engineering, **16**, 284–295, 1969.

25. O. Frank, *Die Theorie der Pulswellen*, Zeitschrift für Biologie, **85**, 91–130, 1926.

26. D.W. Schoendorfer, A.H. Shapiro, *The collapsible tube as a prosthetic vocal source*, Proceedings San Diego Biomedical Symposium, **16**, pp. 349–356, San Diego, California, 1977.

27. A.I. Katz, Y. Chen, A.H. Moreno, *Flow through a collapsible tube (experimental analysis and mathematical model)*, Biophysical Journal, **9**, 1261–1279, 1969.

28. T.J. Pedley, *The Fluid Mechanics of Large Blood Vessels*, Cambridge University Press, Cambridge, UK, 1980.

29. A.H. Shapiro, *Steady flow in collapsible tubes*, Journal of Biomechanical Engineering, **99**, 126–147, 1977.

30. C. Cancelli, T.J. Pedley, *A separated-flow model for collapsible-tube oscillations*, Journal of Fluid Mechanics, **157**, 375–404, 1985.

31. P. Morgan, K.H. Parker, *A mathematical model of flow through a collapsible tube. I. Model and steady flow results*, Journal of Biomechanics, **22**, 1263–1270, 1989.

32. J.R. Womersley, *An elastic tube theory of pulse transmission and oscillatory flow in mammalian arteries*, Wright Air Development Center, Wright-Patterson Air Force Base, Technical Report TR-56-614, Dayton, Ohio, 1957.

33. B.N. Schaaf, D.H. Abbrecht, *Digital computer simulation of the human systemic arterial pulse wave transmission: a nonlinear model*, Journal of Biomechanics, **5**, 345–364, 1972.

34. J.H. Olsen, A.H. Shapiro, *Large-amplitude unsteady flow in liquid-filled elastic tubes*, Journal of Fluid Mechanics, **29**, 513–538, 1967.

35. O.E. Jensen, T.J. Pedley, *The existence of steady flow in a collapsed tube*, Journal of Fluid Mechanics, **206**, 333–374, 1989.

36. O.E. Jensen, *Instabilities of flow in a collapsed tube*, Journal of Fluid Mechanics, **220**, 623–659, 1990.

37. W.M. Bayliss, *On the local reactions of the arterial wall to changes of internal pressure*, Journal of Physiology, **28**, 220–231, 1902.

38. S.A. Regirer, N.H. Shadrina, *Elementary model of a vessel with the wall sensitive to mechanical stimuli*, Biophysics, **47**, 908–913, 2002 [in Russian].

39. S.A. Regirer, I.M. Skobeleva, *Flow of a viscous liquid in a deformable tube with porous wall*, Izvestija Akademy Nauk of the SSSR, Ser. Mekhanika Zhidkosti i Gaza, **3**, 118–131, 1971 [in Russian].

40. S.A. Regirer, I.M. Rutkevich, P.I. Usik, *A model of vascular tone*, Mechanics of polymers, **4**, 585–589, 1975 [in Russian].

41. E.E. Kireeva, B.N. Klochkov, *Nonlinear model of vascular tone*, Mechanics of Composite Materials, **5**, 887–894, 1982 [in Russian].

42. X.Y. Luo, T.J. Pedley, *A numerical simulation of unsteady flow in a 2-D collapsible channel*, Journal of Fluids & Structures, **9**, 149–174, 1995.

43. X.Y. Luo, T.J. Pedley, *The effects of wall inertia on flow in a two-dimensional collapsible channel*, Journal of Fluid Mechanics, **363**, 253–280, 1998.

44. X.Y. Luo, T.J. Pedley, *Multiple solutions and flow limitation in collapsible channel flows*, Journal of Fluid Mechanics, **420**, 301–324, 2000.

45. X.Y. Luo, Z. Cai, W.G. Li, T.J. Pedley, *The cascade structure of linear instability in collapsible channel flows*, Journal of Fluid Mechanics, **600**, 45–76, 2008.

46. Z.X. Cai, X.Y. Luo, *A fluid–beam model for flow in a collapsible channel*, Journal of Fluids and Structures, **17**, 125–146, 2003.

47. A. Marzo, X.Y. Luo, C.D. Bertram, *Axial-Flow Fluid-Structure Interactions. Three-dimensional collapse and steady flow in thick-walled flexible tubes*, Journal of Fluids and Structures, **20**, 817–835, 2005.

48. X.L. Yang, Y. Liu, J.M. Yang, *Fluid-structure interaction in a pulmonary arterial bifurcation*, Journal of Biomechanics, **40**, 2694–2699, 2007.

49. T.J. Pedley, *Longitudinal tension variation in collapsible channels: a new mechanism for the breakdown of steady flow*, ASME Journal of Biomechanical Engineering, **114**, 60–67, 1992.

50. Y.C. Fung, S.Q. Liu, *Determination of the mechanical properties of the different layers of blood vessels in vivo*, Proceedings of the National Academy of Sciences, **92**, 2169–2173, 1995.

51. G.A. Holzapfel, T.C. Gasser, R.W. Ogden, *Comparison of a multi-layer structural model for arterial walls with a Fung-type model, and issues of material stability*, Journal of Biomechanical Engineering, **126**, 264–275, 2004.

52. R.P. Vito, S.A. Dixon, *Blood vessel constitutive models—1995–2002*, Annual Review of Biomedical Engineering, **5**, 413–439, 2003.

53. T.C. Gasser, R.W. Ogden, G.A. Holzapfel, *Hyperelastic modelling of arterial layers with distributed collagen fibre orientations*, Journal of the Royal Society Interface, **3**, 15–35, 2006.

54. J.D. Hartman, *Structural changes within the media of coronary arteries related to intimal thickening*, American Journal of Pathology, **89**, 13–34, 1977.

55. P.B. Canham, H.M. Finlay, J.G. Dixon, D.R. Boughner, A. Chen, *Measurements from light and polarised light microscopy of human coronary arteries fixed at distending pressure*, Cardiovascular Research, **23**, 973–982, 1989.

56. R.J. Coulson, M.J. Cipolla, L. Vitullo, N.C. Chesler, *Mechanical properties of rat middle cerebral arteries with and without myogenic tone*, Journal of Biomechanical Engineering, **126**, 76–81, 2004.

57. M. Hamadiche, M. Gad-el-Hak, *Spatiotemporal Stability of Flow through Collapsible, viscoelastic tubes*, AIAA Journal, **42**, 772–786, 2004.

58. M. Hamadiche, M. Gad-el-Hak, *Temporal Stability of Flow through Viscoelastic Tubes*, Journal of Fluids & Structures, **16**, 331–359, 2002.

59. M. Hamadiche, *Instabilité absolue et convective de l'écoulement de Poiseuille en conduite viscoélastique*, Comptes Rendus de l'Académie des Sciences, Paris, **330**,769–775, 2002.

60. M. Hamadiche, *Flux d'énergie d'un écoulement de Poiseuille vers la paroi d'un Tube Elastique. a. Modes d'instabilité axisymétrique*, Comptes Rendus de l'Académie des Sciences, Paris, **327**, Série II b, 115–1161, 1999.

61. M. Hamadiche, *Flux d'énergie d'un écoulement de Poiseuille vers la paroi d'un tube élastique. b. Modes d'Instabilité non Axisymétrique*, Comptes Rendus de l'Académie des Sciences, Paris, **327**, Série II b, 116–1170, 1999.

62. M. Hamadiche, *Absolute and convective instabilities of Poiseuille flow in viscoélastic tube*, Euromech Fluid Mechanics Conferences, Toulouse, France, 24–28 August, 2003.

63. M. Hamadiche, N. Kizilova, *Temporal and spatial instabilities of the flow in the blood vessels as multi-layered compliant tubes*, International Journal of Dynamics of Fluids, **1**, 1–23, 2005.

64. M. Hamadiche, N. Kizilova, M. Gad-el-Hak, *Suppression of absolute instabilities in the flow inside a compliant tube*, Communications in Numerical Methods in Engineering, **25**, 505–531, 2009.

65. N. Kizilova, M. Hamadiche, M. Gad-el-Hak, *Flow in compliant tubes: control and stabilization by multilayered coatings*, International Journal of Flow Control, **1**, 199–211, 2009.

66. M. Hamadiche, N. Kizilova, *Flow interaction with composite wall*, Proceedings of the ASME Pressure Vessels and Piping Conference, Vancouver, British Columbia, 23–27 July, 2006.

67. P.W. Carpenter, P.J. Morris, *The hydrodynamic stability of flows over non-isotropic compliant surfaces—Numerical solution of the differential eigenvalue problem*, in *Numerical Methods in Laminar and Turbulent Flows*, pp. 1613–1620, Pineridge Press, Swansea, Wales, UK, 1985.

68. P.W. Carpenter, A.D. Garrad, *The hydrodynamic stability of flows over Kramer-type compliant surfaces, Part 2. Flow-induced surface instabilities*, Journal of Fluid Mechanics, **170**, 199–232, 1986.

69. O.E. Jensen, M. Heil, *High-frequency self-excited oscillations in a collapsible-channel flow*, Journal of Fluid Mechanics, **481**, 235–268, 2003.

70. M. Heil, S.L. Waters, *Transverse flows in rapidly oscillating elastic cylindrical shells*, Journal of Fluid Mechanics, **547**, 185–214, 2006.

71. M. Heil, S.L. Waters, *How rapidly oscillating collapsible tubes extract energy from a viscous mean flow*, Journal of Fluid Mechanics, **601**, 199–227, 2008.

72. M. Heil, J. Boyle, *Self-excited oscillations in three-dimensional collapsible tubes: simulating their onset and large-amplitude oscillations*, Journal of Fluid Mechanics, **652**, 405–426, 2010.

73. P.S. Stewart, M. Heil, S.L. Waters, O.E. Jensen, *Sloshing and slamming oscillations in a collapsible channel flow*, Journal of Fluid Mechanics, **662**, 288–319, 2010.

74. R.J. Whittaker, S.L. Waters, O.E. Jensen, J.H. Boyle, M. Heil, *The energetics of flow through a rapidly oscillating tube. Part 1. General theory*, Journal of Fluid Mechanics, **648**, 83–121, 2010.

75. R.J. Whittaker, M. Heil, J.H. Boyle, O.E. Jensen, S.L. Waters, *The energetics of flow through a rapidly oscillating tube. Part 2. Application to an elliptical tube*, Journal of Fluid Mechanics, **648**, 123–153, 2010.

76. R.J. Whittaker, M. Heil, O.E. Jensen, S.L. Waters, *Predicting the onset of high-frequency self-excited oscillations in elastic-walled tubes*, Proceedings of the Royal Society A, **466**, 3635–3657, 2010.

77. M.E. Rosar, S.P. Charles, *Fluid flow in collapsible elastic tubes: a three-dimensional numerical model*, New York Journal of Mathematics, **7**, 281–302, 2001.

78. B. Liu, D. Tang, *A numerical simulation of viscous flows in collapsible tubes with stenoses*, Applied Numerical Mathematics, **32**, 87–101, 2000.

79. T. Dali, Y. Chun, K. Shunici, D.N. Ku, *Experiment-based numerical simulation of unsteady viscous flow in stenotic collapsible tubes*, Applied Numerical Mathematics, **36**, 299–320, 2001.

80. L. Huang, *Viscous flutter of a finite elastic membrane in Poiseuille flow*, Journal of Fluids and Structures, **15**, 1061–1088, 2001.

81. D. Tang, C. Yang, H. Walker, S. Kobayashi, D.N. Ku, *Simulating cyclic artery compression using a 3D unsteady model with fluid–structure interactions*, Computers and Structures, **80**, 1651–1665, 2002.

82. Y. Zhu, X.Y. Luo, R.W. Ogden, *Nonlinear axisymmetric deformations of an elastic tube under external pressure*, European Journal of Mechanics – A/Solids, **29**, 216–229, 2010.

83. V. Oruç, M.Ö. Çarpnlioğlu, *Theoretical approximations to analyse the onset of self-excited oscillations in flow through collapsible tubes*, Journal of Mechanical Engineering Science, **224**, 337–343, 2010.

84. Y. Zhao, A. Forhad, *General method for simulation of fluid flows with moving and compliant boundaries on unstructured grids*, Computer Methods in Applied Mechanics and Engineering, **192**, 4439–4466, 2003.